nanomaterials

MDPI

Article

Quantifying Nonadiabaticity in Major Families of Superconductors

Evgueni F. Talantsev [1,2]

[1] M. N. Miheev Institute of Metal Physics, Ural Branch, Russian Academy of Sciences, 18 S. Kovalevskoy Str., 620108 Ekaterinburg, Russia; evgeny.talantsev@imp.uran.ru; Tel.: +7-912-676-0374
[2] NANOTECH Centre, Ural Federal University, 19 Mira Str., 620002 Ekaterinburg, Russia

Abstract: The classical Bardeen–Cooper–Schrieffer and Eliashberg theories of the electron–phonon-mediated superconductivity are based on the Migdal theorem, which is an assumption that the energy of charge carriers, $k_B T_F$, significantly exceeds the phononic energy, $\hbar\omega_D$, of the crystalline lattice. This assumption, which is also known as adiabatic approximation, implies that the superconductor exhibits fast charge carriers and slow phonons. This picture is valid for pure metals and metallic alloys because these superconductors exhibit $\frac{\hbar\omega_D}{k_B T_F} < 0.01$. However, for n-type-doped semiconducting $SrTiO_3$, this adiabatic approximation is not valid, because this material exhibits $\frac{\hbar\omega_D}{k_B T_F} \cong 50$. There is a growing number of newly discovered superconductors which are also beyond the adiabatic approximation. Here, leaving aside pure theoretical aspects of nonadiabatic superconductors, we classified major classes of superconductors (including, elements, A-15 and Heusler alloys, Laves phases, intermetallics, noncentrosymmetric compounds, cuprates, pnictides, highly-compressed hydrides, and two-dimensional superconductors) by the strength of nonadiabaticity (which we defined by the ratio of the Debye temperature to the Fermi temperature, $\frac{T_\theta}{T_F}$). We found that the majority of analyzed superconductors fall into the $0.025 \leq \frac{T_\theta}{T_F} \leq 0.4$ band. Based on the analysis, we proposed the classification scheme for the strength of nonadiabatic effects in superconductors and discussed how this classification is linked with other known empirical taxonomies in superconductivity.

Keywords: nonadiabatic effects in superconductors; Heusler alloys; Laves phases; magic-angle twisted bilayer graphene; hydrogen-rich superconductors

Citation: Talantsev, E.F. Quantifying Nonadiabaticity in Major Families of Superconductors. *Nanomaterials* **2023**, *13*, 71. https://doi.org/10.3390/nano13010071

Academic Editor: Yassine Slimani

Received: 2 December 2022
Revised: 17 December 2022
Accepted: 19 December 2022
Published: 23 December 2022

1. Introduction

The majority of experimental works in superconductivity utilize the classical Bardeen–Cooper–Schrieffer (BCS) [1] and Migdal–Eliashberg (ME) [2,3] theories as primary tools to analyze measured data. However, it should be clarified that these theories are valid for superconductors which satisfy the condition designated by the Born–Oppenheimer–Migdal approximation [4]:

$$\frac{\hbar\omega_D}{k_B T_F} = \frac{T_\theta}{T_F} = \left.\frac{88\ \mathrm{K}}{1.1 \times 10^5\ \mathrm{K}}\right|_{Pb} = 8 \times 10^{-4} \ll 1 \quad (1)$$

where $\hbar$ is the reduced Planck constant, ω_D is the Debye frequency, k_B is the Boltzmann constant, T_θ is the Debye temperature, T_F is the Fermi temperature, and data for lead were reported by Poole [5]. The Born–Oppenheimer–Migdal approximation allows the separation of electronic and ionic motions in metals, because Equation (1) implies that the conductor exhibits fast charge carriers (for which characteristic energy scale is related to the Fermi temperature, T_F) and relatively slow phonons (for which characteristic energy scale is related to the Debye temperature, T_θ).

However, Equation (1) satisfies for many, but not for all superconductors, and the first discovered superconductor for which Equation (1) was found to be violated is *n*-type doped semiconducting $SrTiO_3$ [6]:

$$\frac{\hbar\omega_D}{k_B T_F} = \frac{T_\theta}{T_F} = \left.\frac{627\text{ K}}{13\text{ K}}\right|_{SrTiO_3} = 48 \gg 1 \quad (2)$$

where data for $SrTiO_3$ is taken from [7,8]. The theoretical description of the superconductivity in materials, in which the charge carriers and the lattice vibrations exhibit characteristic energy scales similar to Equation (2), is complicated, and the general designation of these superconductors are as nonadiabatic superconductors [9–16]. This theory [9–16] provides a general equation for the superconducting transition temperature, T_c, in nonadiabatic superconductors [9]: $T_c = 1.134 \times \frac{\varepsilon_F}{k_B} \times e^{-\frac{1}{\lambda_{nad}}}$, where ε_F is the Fermi energy, and λ_{nad} is the coupling strength constant in nonadiabatic superconductors, which serves a similar role to the electron–phonon coupling strength, λ_{e-ph}, in the BCS [1] and ME [2,3] theories. In addition, one of the primary fundamental theoretical problems is calculating this constant with acceptable accuracy to describe the experiment [4–16].

For experimentalists, it is important to have a simple practical routine to establish the strength of nonantiadiabatic effects in newly discovered superconductors. The most obvious parameter, which serves as an experimentally measured value to quantify the strength of nonantiadiabaticity, is the $\frac{T_\theta}{T_F}$ ratio. For practical use of this criterion, there is a need for the taxonomy of possible $\frac{T_\theta}{T_F}$ values.

To establish the taxonomy, we performed the analysis for a broad a range as possible of superconductors; these range from two- to three-dimensional materials, from elements to compounds of up to five elements, from low-T_c (with $T_c \sim 0.1$ K) to record high-T_c (with $T_c = 240$ K) hydrides, and from materials that exhibit a high order of crystalline lattice symmetry to the materials with low symmetry. Namely, we tried to cover all superconductors for which primary characteristic parameters (apart T_c, T_θ, and T_F), such as the London penetration depth, $\lambda(0)$, the coherence length, $\xi(0)$, the amplitude of the superconducting energy gap, $\Delta(0)$, and the electron–phonon coupling strength constant, λ_{e-ph}, were established. In the results, we presented the analysis of more than 40 superconductors within the families of main superconductors.

Based on our analysis, we proposed the following classification scheme:

$$\begin{cases} \frac{T_\theta}{T_F} < 0.025 \rightarrow \textit{adiabatic superconductor}; \\ 0.025 \lesssim \frac{T_\theta}{T_F} \lesssim 0.4 \rightarrow \textit{moderately strong nonadiabaticity}; \\ 0.4 < \frac{T_\theta}{T_F} \rightarrow \textit{nonadiabatic superconductor}. \end{cases} \quad (3)$$

One of our findings is that for weakly nonadiabatic superconductors (i.e., for materials exhibited $0.025 \leq \frac{T_\theta}{T_F} \lesssim 0.4$), the predicting power of the BCS-ME theories (for instance, the prediction of the superconducting transition temperature) is reasonably accurate. However, all these superconductors are located outside of the BCS corner in the Uemura plot.

We also showed how the proposed classification scheme is linked to other known empirical scaling laws and taxonomies in superconductivity [13,17–21]; meanwhile, the search for the link of the proposed taxonomy with the recently reported big data [22,23] is under progress.

2. Utilized Models

Proposed taxonomy is based on the knowledge of three fundamental temperatures of the superconductor, which are T_c, T_θ, and T_F. The superconducting transition temperature, T_c, is directly measured in either temperature resistance or in magnetization experiments. It is also important to mention the primary experimental techniques and theoretical models utilized to deduce the Debye temperature, T_θ, and the Fermi temperature, T_F, in superconductors.

There are two primary techniques to determine the Debye temperature, T_θ. One technique is to analyze the measured temperature-dependent normal-state specific heat, $C_p(T)$, from which the electronic specific heat coefficient, γ_n, and the Debye temperature, T_θ, are deduced (see, for instance [24–26]):

$$\frac{C_p(T)}{T} = \gamma_n + \beta T^2 + \alpha T^4 \tag{4}$$

where β is the Debye law lattice heat-capacity contribution, and α is from higher order lattice contributions. The Debye temperature can be calculated:

$$T_\theta = \left(\frac{12\pi^4 Rp}{5\beta}\right)^{\frac{1}{3}} \tag{5}$$

where R is the molar gas constant, and p is the number of atoms per formula unit.

Another technique is to fit normal-state temperature dependent resistance, $R(T)$, to the Bloch–Grüneisen (BG) equation [24–28]:

$$R(T) = \frac{1}{\frac{1}{R_{sat}} + \frac{1}{R_0 + A \times \left(\frac{T}{T_\theta}\right)^5 \times \int_0^{\frac{T_\theta}{T}} \frac{x^5}{(e^x-1)(1-e^{-x})} \cdot dx}} \tag{6}$$

where, R_{sat} is the saturated resistance at high temperatures which is temperature independent, R_0 is the residual resistance at $T \to 0\,\mathrm{K}$, and A is free fitting parameter. Many research groups utilized both techniques (i.e., Equations (4)–(6)) to deduce T_θ [24–27,29].

From the measured T_c and the deduced T_θ, one can derive the electron–phonon coupling constant, λ_{e-ph}, as a root of either the original McMillan equation [30], or its recently revisited form [27]:

$$T_c = \left(\frac{1}{1.45}\right) \times T_\theta \times e^{-\left(\frac{1.04(1+\lambda_{e-ph})}{\lambda_{e-ph}-\mu^*(1+0.62\lambda_{e-ph})}\right)} \times f_1 \times f_2^* \tag{7}$$

$$f_1 = \left(1 + \left(\frac{\lambda_{e-ph}}{2.46(1+3.8\mu^*)}\right)^{3/2}\right)^{1/3} \tag{8}$$

$$f_2^* = 1 + (0.0241 - 0.0735 \times \mu^*) \times \lambda_{e-ph}^2 \tag{9}$$

where μ^* is the Coulomb pseudopotential, $0.10 \lesssim \mu^* \lesssim 0.15$ [27,30].

There are several experimental techniques to derive the Fermi temperature, T_F, from experimental data. One of these techniques is to measure the temperature dependent Seebeck coefficient, $S(T)$, and fit a measured dataset to the equation [8]:

$$\left|\frac{S(T)}{T}\right| = \frac{\pi^2}{3}\frac{k_B}{e}\frac{1}{T_F} \tag{10}$$

Another approach is to measure the magnetic quantum oscillations [31], from which the magnitude of charge carrier mass, $m^* = m_e\left(1 + \lambda_{e-ph}\right)$ (where m_e is bare mass of electron), together with the size of the Fermi wave vector, k_F, can be obtained and plugged into [31]:

$$T_F = \frac{\hbar^2}{2k_B}\frac{k_F^2}{m^*} \tag{11}$$

An alternative approach is based on the extraction of the charge carriers mass, m^*, and density, n, as two of four parameters from the simultaneous analysis of $C_p(T)$, $R(T)$, the muon spin relaxation (μSR), the lower critical field data, $B_{c1}(T)$, and the upper critical

field data, $B_{c2}(T)$ [32], and plugging these parameters into the equation for an isotropic spherical Fermi surface [32]:

$$T_F = \frac{\hbar^2}{2k_B}\frac{1}{m^*}\left(3\pi^2 n_s\right)^{\frac{2}{3}} \quad (12)$$

where n_s is bulk charge curriers density at $T \to 0\ K$. For 3D superconductors, n_s is given by the equation [33]:

$$n_s(0) = \frac{m^*}{\mu_0 e^2}\frac{1}{\lambda^2(0)} \quad (13)$$

where μ_0 is the permeability of free space, l is the charge carrier mean free path, $\lambda(0)$ is the ground state London penetration depth, and $\xi(0)$ is the ground state coherence length.

It should be noted that $\lambda(0)$ can be also deduced from the ground state lower critical field [28,34]:

$$B_{c1}(0) = \frac{\phi_0}{4\pi}\frac{ln\left(1+\sqrt{2}\kappa(0)\right)}{\lambda^2(0)} \quad (14)$$

where $\kappa(0) = \frac{\lambda(0)}{\xi(0)}$ is the ground state Ginzburg–Landau parameter.

For two dimensional (2D) superconductors, T_F can be determined from μSR measurements and crystallographic data [18]:

$$T_F = \frac{\pi\hbar^2}{k_B}\frac{1}{m^*}n_s \times c_{int} \quad (15)$$

where c_{int} is the average distance between superconducting planes.

If measuring techniques are limited to the magnetoresistance measurements, $R(T,B)$ (which was the case in the field of highly-compressed near-room temperature superconductors (NRTS) [35–50], until recent experimental progress by Minkov et al. [51,52]), T_F can be estimated by the equation [53]:

$$T_F = \frac{\pi^2 m^*}{2k_B\hbar^2} \times \xi^2(0) \times \Delta^2(0) \quad (16)$$

where $\Delta(0)$ is the ground state amplitude of the superconducting energy gap, which is varying in a reasonably narrow range $3.2 \leq \frac{2\Delta(0)}{k_B T_c} \leq 5.0$, so that the ballpark value for T_F can be estimated. For instance, $\xi(0)$ can be deduced from magnetoresistance measurements [54] and the electron–phonon coupling strength constant, λ_{e-ph}, can be assumed to be the average value of values calculated by first-principles calculations [55,56].

3. Results

In Table 1, we present data for major groups of superconductors, where data sources for T_c, T_θ, T_F, and other parameters (for instance, λ_{e-ph}) are given.

Table 1. Superconductors and their parameters used in the work. In all calculations (except some original sources, $\mu^* = 0.13$).

Type/Chemical Composition	λ(0) (nm)	ξ(0) (nm)	$\lambda_{e\text{-}ph}$	T_c (K)	T_θ (K)	$\frac{2\Delta(0)}{k_B T_c}$	T_F (10^3 K)	T_θ/T_F
Pure metals								
Aluminium				1.18 [57,58]	394 [5]		136 [5]	2.9×10^{-3}
Aluminium	50 [57]	1550 [58]	0.43 [59]	1.18 [57,58]	394 [5]	3.535 [59]	18.9 (Equation (12))	2.1×10^{-2}
Tin				3.72 [58]	170 [5]		118 [5]	1.4×10^{-3}

Table 1. *Cont.*

Type/Chemical Composition	λ(0) (nm)	ξ(0) (nm)	$\lambda_{e\text{-}ph}$	T_c (K)	T_θ (K)	$\frac{2\Delta(0)}{k_B T_c}$	T_F (10^3 K)	T_θ/T_F
Tin	77 [60]	180 [58]	0.72 [59]	3.72 [58]	170 [5]	3.705 [59]	10.0 (Equation (12))	1.2×10^{-2}
Lead				7.20 [58]	88 [5]		110 [5]	8×10^{-4}
Lead	64 [60]	87 [58]	1.55 [59]	7.20 [60]	88 [5]	4.497 [59]	11.2 (Equation (12))	7.8×10^{-3}
Niobium				9.25 [58]	265 [5]		61.8 [5]	4.3×10^{-3}
Niobium	52 [58]	39 [58]	0.98 [59]	9.25 [58]	265 [5]	3.964 [59]	16.1 (Equation (12))	1.6×10^{-2}
Gallium	52 [58]	39 [58]	2.25 [59]	1.09 [5,32,58,59]	325 [5,32,58,59]		120 [5,32,58]	2.7×10^{-3}
A15 Alloys								
Nb_3Sn	124 [61]	3.6 [61]	1.8 [62]	17.9 [61]	234 [61]	4.2 [62]	4.5 (Equation (12))	5.2×10^{-2}
V_3Si	62 [62]	3.3 [62]	0.96 [62]	16.4 [63]	297 [64]	3.7 [62]	12.8 (Equation (12))	2.3×10^{-2}
Nb_3Ge	90 [58]	3.0 [58]	1.60 [59]	23.2 [58]	302 [65]	4.364 [59]	7.1 (Equation (12))	4.3×10^{-2}
Heusler alloys								
$ZrNi_2Ga$	350 [66]	15 [66]	0.551 [66]	2.85 [66]	300 [66]		1.4 (Equation (12))	2.2×10^{-1}
YPd_2Sn	196 [67]	19 [67]	0.70 [67]	4.7 [67]	210 [67]	4.1 [67]	2.9 (Equation (12))	7.2×10^{-2}
$HfPd_2Al$	225 [67]	13 [67]	0.68 [67]	3.66 [67]	182 [67]	3.74 [67]	2.4 (Equation (12))	7.5×10^{-2}
Noncentrosymmetric								
$Nb_{0.5}Os_{0.5}$	654 [68]	7.8 [68]	0.53 [68]	3.07 [68]	367 [68]	3.62 [68]	0.60 (Equation (12))	6.1×10^{-1}
Re_6Zr (mSR)	356 [29]	3.7 [29]	0.67 [29]	6.75 [29]	338 [29]	3.72 [29]	1.3	2.6×10^{-1}
Re_6Zr (magnetization)	247 [29]	3.3 [29]	0.67 [29]	6.75 [29]	237 [29]	3.72 [29]	2.1	1.1×10^{-1}
Mo_3Al_2C	376 [69]	4.2 [69]	0.74 (Equations (7)–(9))	9.2 [69]	339 [69]	4.03 [69]	1.2	2.8×10^{-1}
$NbIr_2B_2$ [70]	223	4.5	0.74	7.18	274		2.4	1.1×10^{-1}
$TaIr_2B_2$ [70]	342	4.7	0.70	5.1	230		1.4	1.7×10^{-1}
Re_3Ta [71]			0.62	4.7	321		0.64	5.0×10^{-1}
Laves phases								
$BaRh_2$ [72]	340	8.4	0.80	5.6	178		1.4	1.3×10^{-1}
$SrRh_2$ [72]	229	9.1	0.71	5.4	237		2.3	1.0×10^{-1}
$SrRh_2$ [73]	121	8.6	0.93	5.4	250		5.3	4.7×10^{-2}
$SrIr_2$ [74]	237	7.5	0.84	5.9	180		2.3	8.2×10^{-2}
Intermetallics								
$MgCNi_3$ [75]	248	4.6	0.74 (Equations (7)–(9))	7.6	284		2.1	1.4×10^{-1}
$RuAl_6$ [76]	265	27.7	0.81	1.21	458		1.9	2.4×10^{-1}
Perovskite								
$SrTiO_3$			0.2 [7]	0.086 [8]	690 [77]		1.3×10^{-2} [8]	5.3×10^{1}
Pnictides								
ThFeAsN	375 [78]		1.48 [78]	28.1 [78]	332 [79]		0.47 (Equation (17)) $c_{int} = 8.5$ Å [78]	7.0×10^{-1}
$KCa_2Fe_4As_4F_2$	230 [80]		1.59 [80]	33.4 [80]	366 [80]		1.3 (Equation (17)) $c_{int} = 8.5$ Å [80]	2.9×10^{-1}
$RbCa_2Fe_4As_4F_2$	232 [80]		1.45 [80]	29.2 [80]	332 [80]		1.2 (Equation (17)) $c_{int} = 8.5$ Å [80]	2.8×10^{-1}
$CsCa_2Fe_4As_4F_2$	244 [80]		1.44 [80]	28.3 [80]	344 [80]		1.1 (Equation (17)) $c_{int} = 8.5$ Å [80]	3.1×10^{-1}

Table 1. *Cont.*

Type/Chemical Composition	λ(0) (nm)	ξ(0) (nm)	$\lambda_{e\text{-}ph}$	T_c (K)	T_θ (K)	$\frac{2\Delta(0)}{k_B T_c}$	T_F (10^3 K)	T_θ/T_F
Cuprates								
$YBa_2Cu_3O_7$ [81]	115 [81,82]	2.5 [81]	1.5 [83]	93.2 [81]	437 [7]		3.4 (Equation (17)) $c_{int} = 5.8$ Å [83]	1.2×10^{-1}
$(Y,Dy)Ba_2Cu_3O_7$ [84]	128 [84,85]	2.5 [81]	1.5 [83]	90.4 [84,85]	437 [7]	4.24 [84,85]	2.9 (Equation (17)) $c_{int} = 5.8$ Å [83]	1.5×10^{-1}
$Bi_2Sr_2CaCu_2O_8$ [86]	196 [85]	1.2 [85]	4.7 [7]	82.7 [85]	240 [7]	3.9 [85]	1.2 (Equation (17)) $c_{int} = 6$ Å [83]	2.0×10^{-1}
$Tl_2Ba_2CaCu_2O_8$ [87]	179 [85]	1.2 [85]		103 [85]	425 [88]	4.3 [85]	1.5 (Equation (17)) $c_{int} = 6$ Å [83]	2.9×10^{-1}
$HgBa_2CaCu_2O_8$ [89]	188 [85]	1.6 [85]		120 [85]	525 [88]	3.3 [85]	1.3 (Equation (17)) $c_{int} = 6$ Å [83]	3.9×10^{-1}
$Bi_2Sr_2Ca_2Cu_3O_{10}$ [90]	175 [85]	1.0 [85]	4.5	85 [85]	319 [7]	4.5 [85]	1.5 (Equation (17)) $c_{int} = 6$ Å [83]	2.1×10^{-1}
Bismuthates								
$Ba_{1-x}K_xBiO_3$ (x = 0.4) [91,92]			1.10 [93]	23 [92]	210 [94]	3.8-4.1 [93]	1.5 [92]	1.4×10^{-1}
$Ba_{1-x}K_xBiO_3$ (x = 0.5) [91,92]			1.10 [93]	14 [92]	210 [94]	3.8-4.0 [93]	1.1 [92]	1.9×10^{-1}
2D superconductors								
MATBG [95]	2180 [96]		$\frac{m^*}{m_e} = 0.2$ [96]	1.2 [96]	1864 [97]	4.4 [96]	16.5×10^{-3} (Equation (15)) $c_{int} = 1$ nm	1.1×10^2
MATBG [95]		61.4 [96]	[96]	1.2 [96]	1864 [97]	4.4 [96]	28.6×10^{-3} (Equation (16))	6.5×10^1
Li-doped graphene, LiC_6 [98]			0.61 [99]	5.9 [98]	2240 [99]		15.5 [99]	1.45×10^{-1}
$IrTe_2$ [100] (sample thickness is 21 nm)	600 [100]	75 [100]		1.6 [100]		5.46 [100]	0.118 (Equation (15)) $c_{int} = 0.54$ nm	
Ionic Salt								
CsI (P = 206 GPa) [101]			0.445 [102]	1.1 [101]	339 [102]		$(20 \pm 4) \times 10^{-2}$ [102]	17 ± 4 [102]
NRTS hydrides								
H_3S (P = 155 GPa) [35]	37 [52]	1.9 [54]	2.2 [103]	197 [103]	1427 [103]		21.6 (Equation (12)) and [104]	6.6×10^{-2}
H_3S (P = 155 GPa) [35]		1.9 [54]	1.76 [55,56]	197 [103]	1427 [103]	3.55 [53]	10 ± 3 (Equation (16)) and [104]	$(1.4 \pm 0.3) \times 10^{-1}$
LaH_{10} (P = 150 GPa) [36]	30 [51]	1.5 [51]	2.77 [27]	240 [27]	1310 [27]		27.0 (Equation (12))	2.7×10^{-2}
$La_{1-x}Nd_xH_{10}$ (x = 0.15) (P = 180 GPa) [48]		2.3 [105]	1.65 [105]	122 [105]	1156 [105]	4.0 [105]	4.4 [105] (Equation (16))	2.6×10^{-1}
Compressed oxygen								
ζ-O_2 (P = 115 GPa) [106]		42 [107]	0.42 [107]	0.64 [107]	306 [107]		3.5×10^{-2} [107] (Equation (16))	8.7

In Figure 1, we show the T_c vs.T_F dataset in a log–log plot, which is the traditional data representation in the well-known Uemura plot [18].

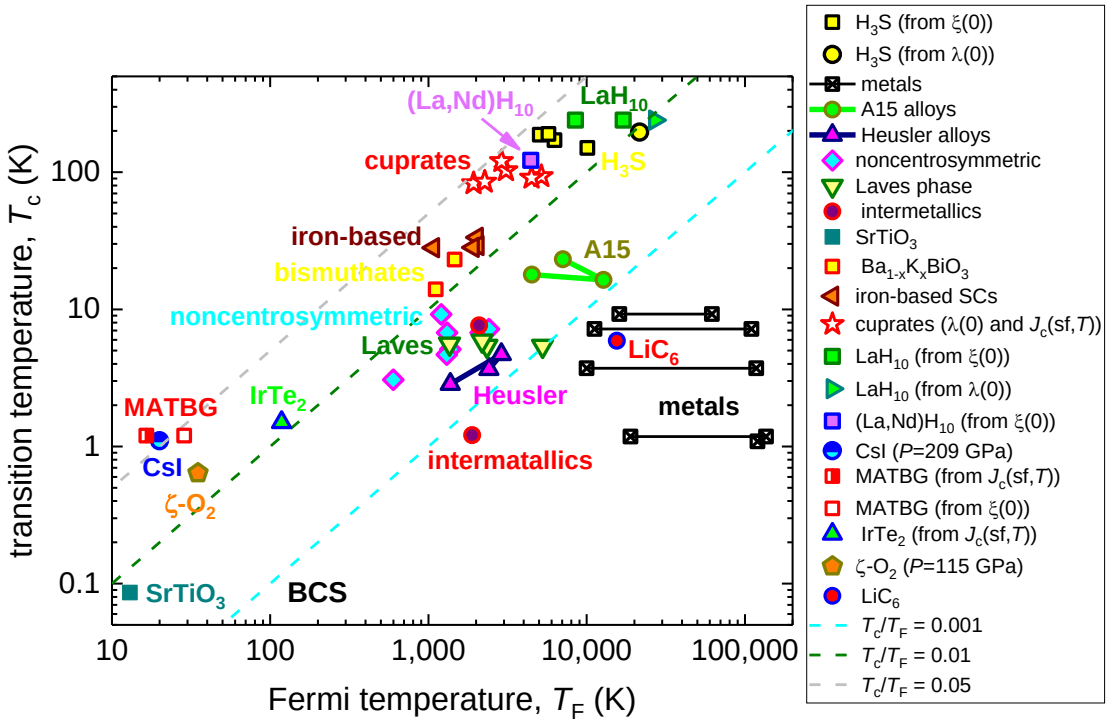

Figure 1. Uemura plot (T_c vs. T_F) for primary superconducting families. References on original data (T_c and T_F) can be found in Table 1.

In Figure 2, we represent the same superconducting materials, but here we display the λ_{e-ph} vs. $\frac{T_\theta}{T_F}$ dataset in a semi-log plot. To our best knowledge, the λ_{e-ph} vs. $\frac{T_\theta}{T_F}$ plot was first plotted by Pietronero et al. [13] in linear–linear scales. However, because the $\frac{T_\theta}{T_F}$ ratio for main families of superconductors is varied within four orders of magnitude (Table 1), and $0.4 \leq \lambda_{e-ph} \leq 3.0$, it is more suitable to use the semi-log plot (Figure 2).

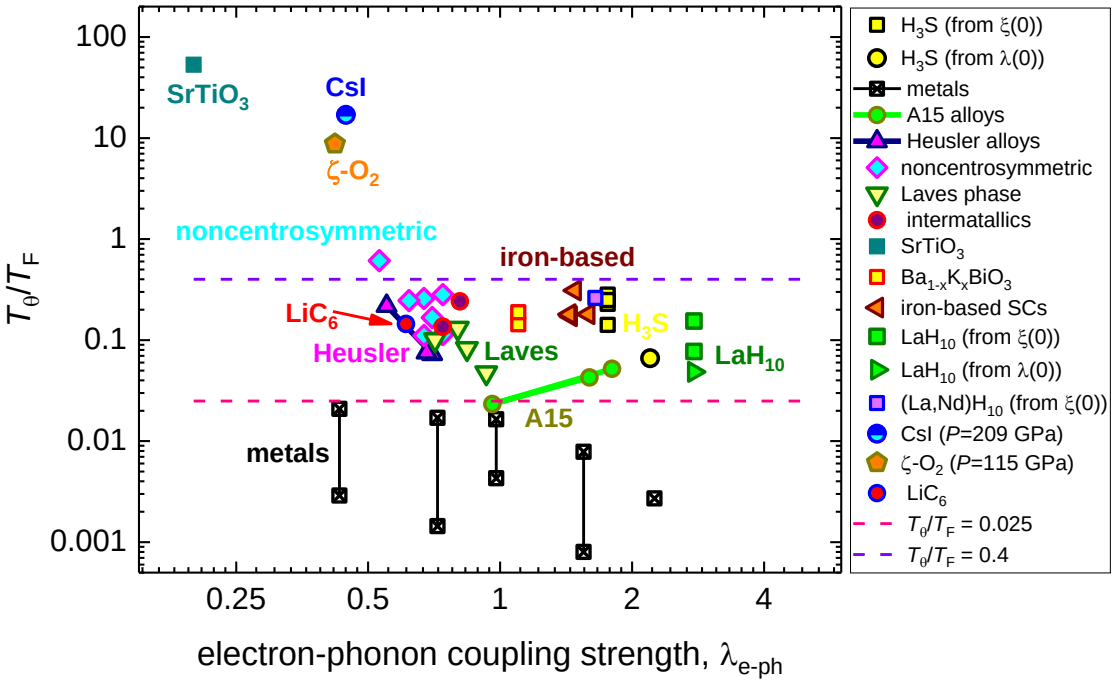

Figure 2. Plot of $\frac{T_\theta}{T_F}$ vs. λ_{e-ph} for primary superconducting families. This type of plot proposed by Pietronero et al. [13]. References for original data (T_θ, λ_{e-ph}, T_F) can be found in Table 1.

Finally, in Figure 3, we represented the same superconducting materials, but here we displayed the T_c vs. $\frac{T_\theta}{T_F}$ dataset in a log–log plot. This type of plot was chosen because as T_c, as $\frac{T_\theta}{T_F}$ are varied within several orders of magnitude.

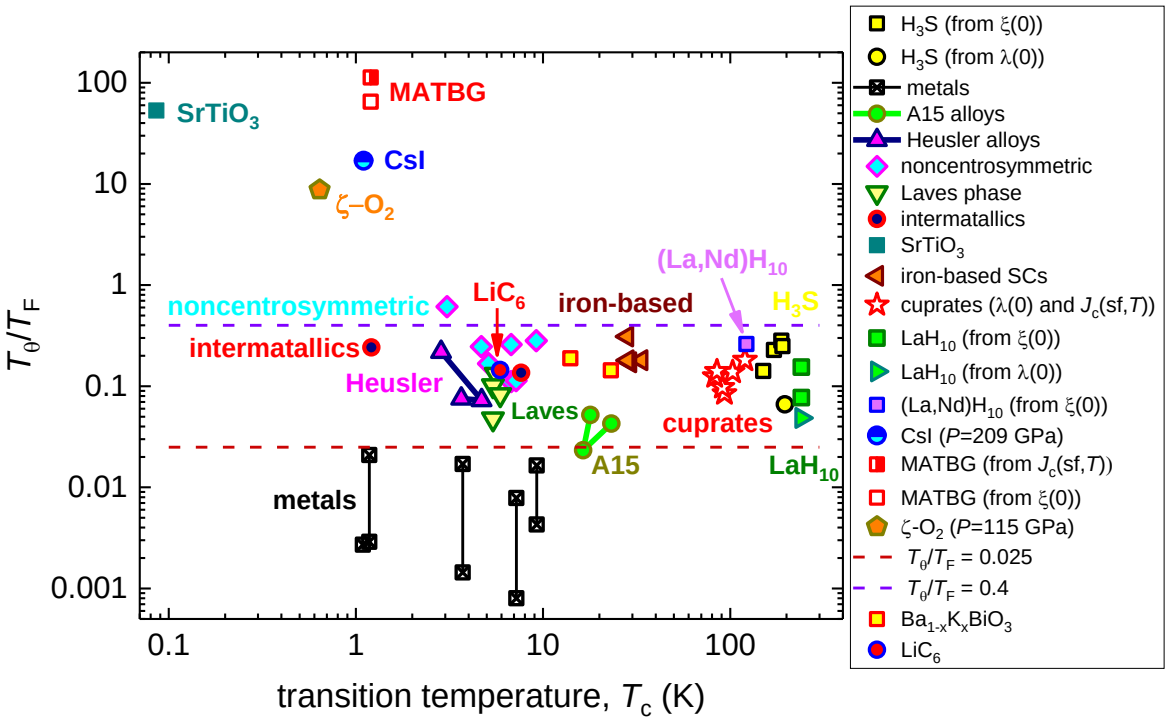

Figure 3. Plot $\frac{T_\theta}{T_F}$ vs. T_c for primary superconducting families. References on original data (T_θ, T_c, T_F) can be found in Table 1.

4. Discussion

The family of near-room temperature superconductors (NRTS) is represented in Table 1 and Figure 1 by H_3S (P = 155 GPa), SnH_{12} (P = 190 Gpa), and $La_{1-x}Nd_xH_{10}$ (x = 0.09, P = 180 Gpa). Two independent approaches were used to perform calculations in H_3S:

1. T_F was calculated based on Equations (12) and (13). In these calculations $\lambda(0) = 37$ nm (extracted from the analysis of DC magnetization experiments reported by Minkov et al. [51,52]) was used.
2. T_F was calculated based Equations (6)–(9) and (18), in which utilized $\xi(0)$ values were extracted [53] from magnetoresistance measurements reported by Mozaffari et al. [54]).

It should be noted that, in both approaches, the electron–phonon coupling strength constant, λ_{e-ph}, was assumed to be $\lambda_{e-ph} = 1.76$, which is the average value of values calculated by first-principles calculations [55,56], and values extracted from experimental $R(T)$ data [27].

It can be seen in Table 1 and Figure 1 that the calculated T_F values for H_3S, by two alternative approaches, are in a very good agreement with each other. To demonstrate the acceptable level of variation in T_F values for the same material, in Table 1 and Figure 1 we present the results of the calculations for pure metals, where T_F was calculated by the two approaches mentioned above and the use of experimental data reported by different research groups.

T_F in HTS cuprates were calculated by the Equations (13) and (15), which do not require the knowledge of the electron–phonon coupling constants, λ_{e-ph}. This is despite Ledbetter et al. [7] reporting the so-called effective electron–phonon coupling strength, $\lambda_{e-ph,eff}$, from which the effective mass can be deduced, $m^* = \left(1 + \lambda_{e-ph,eff}\right) \times m_e$.

In addition, it should be noted that for $YBa_2Cu_3O_7$, Uemura [83] reported the relation [83]:

$$\frac{m^*}{m_e} = 2.5 \tag{17}$$

from which $\lambda_{e-ph} = 1.5$ can be derived. Calculated values are in a reasonable agreement with experimental $\frac{m^*}{m_e}$ values reported by several research groups [108–110] in $YBa_2Cu_3O_{7-x}$.

However, because the phenomenology of the electron–phonon mediated superconductivity cannot describe the superconducting state in cuprates, and the T_θ for cuprates were taken as experimental values (see, for instance, report by Ledbetter et al. [7,88]), all cuprate superconductors are shown in Figures 1 and 3 and are not shown in Figure 2.

It should be mentioned that the result of the T_F calculation in MATBG (Table 1), $T_F = 16.5$ K, which was primarily based on the London penetration depth, $\lambda(0) = 1860$ nm, was deduced in Ref. [96] from the self-field critical current density, $J_c(sf, T)$, by the approach proposed by us [84]:

$$J_c(sf, T) = \frac{\phi_0}{4\pi\mu_0} \frac{ln\left(1 + \sqrt{2}\kappa(T)\right)}{\lambda^3(T)} \tag{18}$$

The remarkable agreement of the deduced value, $T_F = 16.5$ K, and the value reported in the original work on MATBG by Cao et al. [95], $T_F = 17$ K, which was calculated based on normal state charge carriers density in MATBG, independently validates our primary idea [84] about the fundamental nature of the self-field critical current in weak-links samples [84,85,111]. This concept was recently proven by Paturi and Huhtinen [112], who utilized the fact that the London penetration depth, $\lambda(0)$, in real samples, depends on the mean free-path of charge carriers, l:

$$\lambda(0) = \lambda_{clean\ limit}(0)\sqrt{1 + \frac{\xi(0)}{l}} \tag{19}$$

where $\lambda(0)$ is the effective penetration depth, and $\lambda_{clean\ limit}(0)$ is the penetration depth in samples, exhibiting a very long mean free-path, $l \gg \xi(0)$. Paturi and Huhtinen [112] varied l in $YBa_2Cu_3O_{7-x}$ films and showed that the change in $J_c(st, T)$ satisfies Equations (18) and (19).

Materials, in which $\lambda(0)$ was deduced by the mean temperature dependent self-field critical current density, $J_c(sf, T)$ (Equation (18)), have designation "$J_c(sf, T)$" in Figures 1–3.

The MATBG does not show in Figure 2, because the derivation of λ_{e-ph} cannot be performed by the used phenomenology: $m^* = \left(1 + \lambda_{e-ph}\right) \times m_e$, because $\frac{m^*}{m_e} = 0.2$ [96]; however, this material is shown in Figures 1 and 3, because λ_{e-ph} is not required for these plots.

Returning back to hydrides, we need to note that Durajski [56] performed first-principles and studied the strength of the nonadiabatic effects in highly-compressed sulfur hydride and phosphorus hydride. Calculations show that the strength of the nonadiabatic effects can be quantified as moderately weak in comparison with the classical nonadiabatic superconductor $SrTiO_3$. This is in a good agreement with our result (see Figure 3 and Table 1), that all deduced $\frac{T_\theta}{T_F}$ values for NRTS are within the range of:

$$0.03 \leq \frac{T_\theta}{T_F} \leq 0.3 \tag{20}$$

Moreover, the classical nonadiabatic superconductor $SrTiO_3$ falls into the intermediate zone between unconventional and BCS superconductors; this is because this material exhibits $\frac{T_c}{T_F} = 0.0066$, and by this criterion, $SrTiO_3$ is similar to the Laves phase materials, intermetallics, A-15 alloys, and Heusler alloys, which cannot be considered to be a correct manifestation of primary uniqueness for this nonadiabatic material.

More unexpectedly, a two dimensional LiC_6 (which is a lithium-doped graphene) superconductor falls into the BCS metals zone in the Uemura plot (Figure 1), despite the fact that this material exhibits reasonable strength in the nonadiabatic effects, $\frac{T_c}{T_F} = 0.15$ [99].

However, in Figures 2 and 3, the outstanding separations of all nonadiabatic superconductors from their adiabatic and moderate nonadiabatic counterparts are clearly manifested.

By looking at the data in Figures 2 and 3, it is easy to recognize that 3/4 (32 of 42) of the analyzed superconductors fall into a reasonably narrow band:

$$0.025 \leq \frac{T_\theta}{T_F} \leq 0.4 \tag{21}$$

Based on this, we proposed that the values in Equation (21) were used as empirical limits for the adiabatic superconductors ($\frac{T_\theta}{T_F} \leq 0.025$), moderate nonadiabatic superconductors ($0.025 \leq \frac{T_\theta}{T_F} \leq 0.4$), and strong nonadiabatic superconductors ($\frac{T_\theta}{T_F} \geq 0.4$).

It also follows from our analysis that all strong nonadiabatic superconductors exhibit low superconducting transition temperatures, $T_c \leq 1.2$ K (Figure 3).

5. Conclusions

In this work, we proposed a new classification scheme to quantify the effects of nonadiabaticity in superconductors. By performing the analysis of experimental data for more than 40 superconductors, which represent the primary families of superconductors, we found that $\frac{3}{4}$ of all analyzed superconductors fall into a narrow $0.025 \leq \frac{T_\theta}{T_F} \leq 0.4$ band. Based on this, we proposed the taxonomy for the strength of the nonadiabatic effects in superconductors.

Funding: This research was funded by the Ministry of Science and Higher Education of the Russian Federation, grant number No. AAAA-A18-118020190104-3 (theme "Pressure"). The research funding from the Ministry of Science and Higher Education of the Russian Federation (Ural Federal University Program of Development within the Priority-2030 Program) is gratefully acknowledged. The APC was funded by MDPI.

Data Availability Statement: Not applicable.

Acknowledgments: The author thanks Luciano Pietronero (Universita' di Roma) for comments about the limitations of the applicability of Migdal–Eliashberg (ME) theory of the electron–phonon mediated superconductivity. The author also thanks Dmitry V. Semenok (Skolkovo Institute of Science and Technology) and Dominik Szczesniak (Jan Dlugosz University in Czestochowa) for reading and commenting on the paper.

Conflicts of Interest: The author declares no conflict of interest.

References

1. Bardeen, J.; Cooper, L.N.; Schrieffer, J.R. Theory of superconductivity. *Phys. Rev.* **1957**, *108*, 1175–1204. [CrossRef]
2. Migdal, A.B. Interaction between electrons and lattice vibrations in a normal metal. *Sov. Phys. JETP* **1958**, *7*, 996–1001.
3. Eliashberg, G.M. Interactions between electrons and lattice vibrations in a superconductor. *Sov. Phys. JETP* **1960**, *11*, 696–702.
4. Pietronero, L.; Strässler, S.; Grimaldi, C. Nonadiabatic superconductivity. I. Vertex corrections for the electron-phonon interactions. *Phys. Rev. B* **1995**, *52*, 10516–10529. [CrossRef]
5. Poole, C.P. *Handbook of Superconductivity*, 1st ed.; Poole, C.P., Jr., Ed.; Academic Press: New York, NY, USA, 1999; pp. 31–32.
6. Takada, Y. Theory of superconductivity in polar semiconductors and its application to n-type semiconducting $SrTiO_3$. *J. Phys. Soc. Jpn.* **1980**, *49*, 1267–1275. [CrossRef]
7. Ledbetter, H.; Lei, M.; Kim, S. Elastic constants, Debye temperatures, and electron-phonon parameters of superconducting cuprates and related oxides. *Phase Transit.* **1990**, *23*, 61–70. [CrossRef]
8. Lin, X.; Zhu, Z.; Fauque, B.; Behnia, K. Fermi surface of the most dilute superconductor. *Phys. Rev. X* **2013**, *3*, 021002. [CrossRef]
9. Takada, Y. Plasmon mechanism of superconductivity in two- and three-dimensional electron systems. *J. Phys. Soc. Jpn.* **1978**, *45*, 786–794. [CrossRef]
10. Grimaldi, C.; Pietronero, L.; Strässler, S. Nonadiabatic superconductivity. II. Generalized Eliashberg equations beyond Migdal's theorem. *Phys. Rev. B* **1995**, *52*, 10530–10546. [CrossRef]

11. Grimaldi, C.; Cappelluti, E.; Pietronero, L. Isotope effect on m^* in high T_c materials due to the breakdown of Migdal's theorem. *Europhys. Lett.* **1998**, *42*, 667–672. [CrossRef]
12. Cappelluti, E.; Ciuchi, S.; Grimaldi, C.; Pietronero, L.; Strässler, S. High T_c superconductivity in MgB_2 by nonadiabatic pairing. *Phys. Rev. Lett.* **2002**, *88*, 117003. [CrossRef]
13. Pietronero, L.; Boeri, L.; Cappelluti, E.; Ortenzi, L. Conventional/unconventional superconductivity in high-pressure hydrides and beyond: Insights from theory and perspectives. *Quantum Stud. Math. Found.* **2018**, *5*, 5–21. [CrossRef]
14. Klimin, S.N.; Tempere, J.; Devreese, J.T.; He, J.; Franchini, C.; Kresse, G. Superconductivity in $SrTiO_3$: Dielectric function method for non-parabolic bands. *J. Supercond. Nov. Magn.* **2019**, *32*, 2739–2744. [CrossRef]
15. Gor'kov, L.P. Phonon mechanism in the most dilute superconductor n-type $SrTiO_3$. *Proc. Natl. Acad. Sci. USA* **2016**, *113*, 4646–4651. [CrossRef] [PubMed]
16. Kresin, V.Z.; Wolf, S.A. *Colloquium*: Electron-lattice interaction and its impact on high T_c superconductivity. *Rev. Mod. Phys.* **2009**, *81*, 481–501. [CrossRef]
17. Harshman, R.; Fiory, A.T. High-T_c superconductivity in hydrogen clathrates mediated by Coulomb interactions between hydrogen and central-atom electrons. *J. Supercond. Nov. Magn.* **2020**, *33*, 2945–2961. [CrossRef]
18. Uemura, Y.J. Classifying superconductors in a plot of T_c versus Fermi temperature T_F. *Physical C* **1991**, *185–189*, 733–734. [CrossRef]
19. Talantsev, E.F.; Crump, W.P.; Tallon, J.L. Universal scaling of the self-field critical current in superconductors: From sub-nanometre to millimetre size. *Sci. Rep.* **2017**, *7*, 10010. [CrossRef]
20. Homes, C.C.; Dordevic, S.V.; Strongin, M.; Bonn, D.A.; Liang, R.; Hardy, W.N.; Komiya, S.; Ando, Y.; Yu, G.; Kaneko, N.; et al. A universal scaling relation in high-temperature superconductors. *Nature* **2004**, *430*, 539–541. [CrossRef]
21. Koblischka, R.; Koblischka-Veneva, A. Calculation of T_c of superconducting elements with the Roeser–Huber formalism. *Metals* **2022**, *12*, 337. [CrossRef]
22. Zhang, T.; Jiang, Y.; Song, Z.; Huang, H.; He, Y.; Fang, Z.; Weng, H.; Fang, C. Catalogue of topological electronic materials. *Nature* **2019**, *566*, 475–479. [CrossRef] [PubMed]
23. Xu, Y.; Vergniory, M.G.; Ma, D.-S.; Mañes, J.L.; Song, Z.-D.; Bernevig, B.A.; Regnault, N.; Elcoro, L. Catalogue of topological phonon materials. *arXiv* **2022**, arXiv:2211.11776. [CrossRef]
24. Pyon, S.; Kudo, K.; Matsumura, J.-I.; Ishii, H.; Matsuo, G.; Nohara, M.; Hojo, H.; Oka, K.; Azuma, M.; Garlea, V.O.; et al. Superconductivity in noncentrosymmetric iridium silicide Li_2IrSi_3. *J. Phys. Soc. Jpn.* **2014**, *83*, 093706. [CrossRef]
25. Kudo, K.; Hiiragi, H.; Honda, T.; Fujimura, K.; Idei, H.; Nohara, M. Superconductivity in Mg_2Ir_3Si: A fully ordered Laves phase. *J. Phys. Soc. Jpn.* **2020**, *89*, 013701. [CrossRef]
26. Sobczak, Z.; Winiarski, M.J.; Xie, W.; Cava, R.J.; Klimczuk, T. Superconductivity in the intermetallic compound Zr_5Al_4. *EPL* **2019**, *127*, 37005. [CrossRef]
27. Talantsev, E.F. Advanced McMillan's equation and its application for the analysis of highly-compressed superconductors. *Supercond. Sci. Technol.* **2020**, *33*, 094009. [CrossRef]
28. Talantsev, E.F. The electron–phonon coupling constant and the Debye temperature in polyhydrides of thorium, hexadeuteride of yttrium, and metallic hydrogen phase III. *J. Appl. Phys.* **2021**, *130*, 195901. [CrossRef]
29. Mayoh, D.A.; Barker, J.A.T.; Singh, R.P.; Balakrishnan, G.; Paul, D.M.; Lees, M.R. Superconducting and normal-state properties of the noncentrosymmetric superconductor Re_6Zr. *Phys. Rev. B* **2017**, *96*, 064521. [CrossRef]
30. McMillan, W.L. Transition temperature of strong-coupled superconductors. *Phys. Rev.* **1968**, *167*, 331–344. [CrossRef]
31. Vignolle, B.; Vignolles, D.; LeBoeuf, D.; Lepault, S.; Ramshaw, B.; Liang, R.; Bonn, D.A.; Hardy, W.N.; Doiron-Leyraud, N.; Carrington, A.; et al. Quantum oscillations and the Fermi surface of high-temperature cuprate superconductors. *Comptes Rendus Phys.* **2011**, *12*, 446–460. [CrossRef]
32. Kleiner, R.; Buckel, W. *Superconductivity: An Introduction*, 3rd ed.; Wiley-VCH: Berlin, Germany, 2016.
33. Tinkham, M. *Introduction to Superconductivity.*, 2nd ed.; Dover Publications: New York, NY, USA, 2004.
34. Talantsev, E.F. Critical de Broglie wavelength in superconductors. *Mod. Phys. Lett. B* **2018**, *32*, 1850114. [CrossRef]
35. Drozdov, A.P.; Eremets, M.I.; Troyan, I.A.; Ksenofontov, V.; Shylin, S.I. Conventional superconductivity at 203 kelvin at high pressures in the sulfur hydride system. *Nature* **2015**, *525*, 73–76. [CrossRef] [PubMed]
36. Drozdov, A.P.; Kong, P.P.; Minkov, V.S.; Besedin, S.P.; Kuzovnikov, M.A.; Mozaffari, S.; Balicas, L.; Balakirev, F.F.; Graf, D.E.; Prakapenka, V.B.; et al. Superconductivity at 250 K in lanthanum hydride under high pressures. *Nature* **2019**, *569*, 528–531. [CrossRef] [PubMed]
37. Somayazulu, M.; Ahart, M.; Mishra, A.K.; Geballe, Z.M.; Baldini, M.; Meng, Y.; Struzhkin, V.V.; Hemley, R.J. Evidence for superconductivity above 260 K in lanthanum superhydride at megabar pressures. *Phys. Rev. Lett.* **2019**, *122*, 027001. [CrossRef] [PubMed]
38. Semenok, D.V.; Kvashnin, A.G.; Ivanova, A.G.; Svitlyk, V.; Fominski, V.Y.; Sadakov, A.V.; Sobolevskiy, O.A.; Pudalov, V.M.; Troyan, I.A.; Oganov, A.R. Superconductivity at 161 K in thorium hydride ThH_{10}: Synthesis and properties. *Mater. Today* **2020**, *33*, 36–44. [CrossRef]
39. Chen, W.; Semenok, D.V.; Kvashnin, A.G.; Huang, X.; Kruglov, I.A.; Galasso, M.; Song, H.; Duan, D.; Goncharov, A.F.; Prakapenka, V.B.; et al. Synthesis of molecular metallic barium superhydride: Pseudocubic BaH_{12}. *Nat. Commun.* **2021**, *12*, 273. [CrossRef]

40. Troyan, I.A.; Semenok, D.V.; Kvashnin, A.G.; Sadakov, A.V.; Sobolevskiy, O.A.; Pudalov, V.M.; Ivanova, A.G.; Prakapenka, V.B.; Greenberg, E.; Gavriliuk, A.G.; et al. Anomalous high-temperature superconductivity in YH_6. *Adv. Mater.* **2021**, *33*, 2006832. [CrossRef]
41. Kong, P.; Minkov, V.S.; Kuzovnikov, M.A.; Drozdov, A.P.; Besedin, S.P.; Mozaffari, S.; Balicas, L.; Balakirev, F.F.; Prakapenka, V.B.; Chariton, S.; et al. Superconductivity up to 243 K in yttrium hydrides under high pressure. *Nat. Commun.* **2021**, *12*, 5075. [CrossRef]
42. Ma, L.; Wang, K.; Xie, Y.; Yang, X.; Wang, Y.; Zhou, M.; Liu, H.; Yu, X.; Zhao, Y.; Wang, H.; et al. High-temperature superconducting phase in clathrate calcium hydride CaH_6 up to 215 K at a pressure of 172 GPa. *Phys. Rev. Lett.* **2022**, *128*, 167001. [CrossRef]
43. Semenok, D.V.; Troyan, I.A.; Ivanova, A.G.; Kvashnin, A.G.; Kruglov, I.A.; Hanfland, M.; Sadakov, A.V.; Sobolevskiy, O.A.; Pervakov, K.S.; Lyubutin, I.S.; et al. Superconductivity at 253 K in lanthanum–yttrium ternary hydrides. *Mater. Today* **2021**, *48*, 18–28. [CrossRef]
44. Zhou, D.; Semenok, D.V.; Duan, D.; Xie, H.; Chen, W.; Huang, X.; Li, X.; Liu, B.; Oganov, A.R.; Cui, T. Superconducting praseodymium superhydrides. *Sci. Adv.* **2020**, *6*, eaax6849. [CrossRef] [PubMed]
45. Hong, F.; Shan, P.F.; Yang, L.X.; Yue, B.B.; Yang, P.T.; Liua, Z.Y.; Sun, J.P.; Dai, J.H.; Yu, H.; Yin, Y.Y.; et al. Possible superconductivity at ∼70 K in tin hydride SnH_x under high pressure. *Mater. Today Phys.* **2022**, *22*, 100596. [CrossRef]
46. Chen, W.; Semenok, D.V.; Huang, X.; Shu, H.; Li, X.; Duan, D.; Cui, T.; Oganov, A.R. High-temperature superconducting phases in cerium superhydride with a T_c up to 115 K below a pressure of 1 Megabar. *Phys. Rev. Lett.* **2021**, *127*, 117001. [CrossRef] [PubMed]
47. Osmond, I.; Moulding, O.; Cross, S.; Muramatsu, T.; Brooks, A.; Lord, O.; Fedotenko, T.; Buhot, J.; Friedemann, S. Clean-limit superconductivity in *Im3m* H_3S synthesized from sulfur and hydrogen donor ammonia borane. *Phys. Rev. B* **2022**, *105*, L220502. [CrossRef]
48. Semenok, D.V.; Troyan, I.A.; Sadakov, A.V.; Zhou, D.; Galasso, M.; Kvashnin, A.G.; Ivanova, A.G.; Kruglov, I.A.; Bykov, A.A.; Terent'ev, K.Y.; et al. Effect of magnetic impurities on superconductivity in LaH_{10}. *Adv. Mater.* **2022**, *34*, 2204038. [CrossRef]
49. Bi, J.; Nakamoto, Y.; Zhang, P.; Shimizu, K.; Zou, B.; Liu, H.; Zhou, M.; Liu, G.; Wang, H.; Ma, Y. Giant enhancement of superconducting critical temperature in substitutional alloy $(La,Ce)H_9$. *Nat. Commun.* **2022**, *13*, 5952. [CrossRef]
50. Li, Z.; He, X.; Zhang, C.; Wang, X.; Zhang, S.; Jia, Y.; Feng, S.; Lu, K.; Zhao, J.; Zhang, J.; et al. Superconductivity above 200 K discovered in superhydrides of calcium. *Nat. Commun.* **2022**, *13*, 2863. [CrossRef]
51. Minkov, V.S.; Bud'ko, S.L.; Balakirev, F.F.; Prakapenka, V.B.; Chariton, S.; Husband, R.J.; Liermann, H.P.; Eremets, M.I. Magnetic field screening in hydrogen-rich high-temperature superconductors. *Nat. Commun.* **2022**, *13*, 3194. [CrossRef]
52. Minkov, V.S.; Ksenofontov, V.; Budko, S.L.; Talantsev, E.F.; Eremets, M.I. Trapped magnetic flux in hydrogen-rich high-temperature superconductors. *arXiv* **2022**, arXiv:2206.14108. [CrossRef]
53. Talantsev, E.F. Classifying superconductivity in compressed H_3S. *Mod. Phys. Lett. B* **2019**, *33*, 1950195. [CrossRef]
54. Mozaffari, S.; Sun, D.; Minkov, V.S.; Drozdov, A.P.; Knyazev, D.; Betts, J.B.; Einaga, M.; Shimizu, K.; Eremets, M.I.; Balicas, L. Superconducting phase-diagram of H_3S under high magnetic fields. *Nat. Commun.* **2019**, *10*, 2522. [CrossRef] [PubMed]
55. Errea, I.; Calandra, M.; Pickard, C.J.; Nelson, J.; Needs, R.J.; Li, Y.; Liu, H.; Zhang, Y.; Ma, Y.; Mauri, F. High-pressure hydrogen sulfide from first principles: A strongly anharmonic phonon-mediated superconductor. *Phys. Rev. Lett.* **2015**, *856*, 157004. [CrossRef] [PubMed]
56. Durajski, A.P. Quantitative analysis of nonadiabatic effects in dense H_3S and PH_3 superconductors. *Sci. Rep.* **2016**, *6*, 38570. [CrossRef] [PubMed]
57. Prozorov, R.; Giannetta, R.W.; Carrington, A.; Fournier, P.; Greene, R.L.; Guptasarma, P.; Hinks, D.G.; Banks, A.R. Measurements of the absolute value of the penetration depth in high-T_c superconductors using a low-T_c superconductive coating. *Appl. Phys. Lett.* **2000**, *77*, 4202–4204. [CrossRef]
58. Poole, P.P.; Farach, H.A.; Creswick, R.J.; Prozorov, R. *Superconductivity*; Academic Press: London, UK, 2007; Chapter 1.
59. Carbotte, J.P. Properties of boson-exchange superconductors. *Rev. Mod. Phys.* **1990**, *62*, 1027–1157. [CrossRef]
60. Peabody, G.E.; Meservey, R. Magnetic flux penetration into superconducting thin films. *Phys. Rev. B* **1972**, *6*, 2579–2595. [CrossRef]
61. Guritanu, V.; Goldacker, W.; Bouquet, F.; Wang, Y.; Lortz, R.; Goll, G.; Junod, A. Specific heat of Nb3Sn: The case for a second energy gap. *Phys. Rev. B* **2004**, *70*, 184526. [CrossRef]
62. Orlando, T.P.; McNiff, E.J., Jr.; Foner, S.; Beasley, M.R. Critical fields, Pauli paramagnetic limiting, and material parameters of Nb_3Sn and V_3Si. *Phys. Rev. B* **1979**, *19*, 4545–4561. [CrossRef]
63. Zhang, R.; Gao, P.; Wang, X.; Zhou, Y. First-principles study on elastic and superconducting properties of Nb_3Sn and Nb_3Al under hydrostatic pressure. *AIP Adv.* **2015**, *5*, 107233. [CrossRef]
64. Junod, A.; Muller, J. Comment on specific heat of a transforming V_3Si crystal. *Solid State Commun.* **1980**, *36*, 721–724. [CrossRef]
65. Yamashita, A.; Matsuda, T.D.; Mizuguchi, Y. Synthesis of new high-entropy alloy-type Nb_3(Al, Sn, Ge, Ga, Si) superconductors. *J. Alloys Compd.* **2021**, *868*, 159233. [CrossRef]
66. Winterlik, J.; Fecher, G.H.; Felser, C.; Jourdan, M.; Grube, K.; Hardy, F.; von Löhneysen, H.; Holman, K.L.; Cava, R.J. Ni-based superconductor: Heusler compound $ZrNi_2Ga$. *Phys. Rev. B* **2008**, *78*, 184506. [CrossRef]
67. Klimczuk, T.; Wang, C.H.; Gofryk, K.; Ronning, F.; Winterlik, J.; Fecher, G.H.; Griveau, J.-C.; Colineau, E.; Felser, C.; Thompson, J.D.; et al. Superconductivity in the Heusler family of intermetallics. *Phys. Rev. B* **2012**, *85*, 174505. [CrossRef]

68. Singh, D.; Barker, J.A.T.; Thamizhavel, A.; Hillier, A.D.; McK Paul, D.; Singh, R.P. Superconducting properties and μSR Study of the noncentrosymmetric superconductor $Nb_{0.5}Os_{0.5}$. *J. Phys. Condens. Matter* **2018**, *30*, 075601. [CrossRef] [PubMed]
69. Karki, A.B.; Xiong, Y.M.; Vekhter, I.; Browne, D.; Adams, P.W.; Young, D.P.; Thomas, K.R.; Chan, J.Y.; Kim, H.; Prozorov, R. Structure and physical properties of the noncentrosymmetric superconductor Mo_3Al_2C. *Phys. Rev. B* **2010**, *82*, 064512. [CrossRef]
70. Górnicka, K.; Gui, X.; Wiendlocha, B.; Nguyen, L.T.; Xie, W.; Cava, R.J.; Klimczuk, T. NbIr2B_2 and TaIr2B_2–New low symmetry noncentrosymmetric superconductors with strong spin–orbit coupling. *Adv. Funct. Mater.* **2020**, *31*, 2007960. [CrossRef]
71. Barker, J.A.T.; Breen, B.D.; Hanson, R.; Hillier, A.D.; Lees, M.R.; Balakrishnan, G.; Paul, D.M.; Singh, R.P. Superconducting and normal-state properties of the noncentrosymmetric superconductor Re_3Ta. *Phys. Rev. B* **2018**, *98*, 104506. [CrossRef]
72. Gong, C.; Wang, Q.; Wang, S.; Lei, H. Superconducting properties of $MgCu_2$-type Laves phase compounds $SrRh_2$ and $BaRh_2$. *J. Phys. Condens. Matter* **2020**, *32*, 295601. [CrossRef]
73. Gutowska, S.; Górnicka, K.; Wójcik, P.; Klimczuk, T.; Wiendlocha, B. Strong-coupling superconductivity of $SrIr_2$ and $SrRh_2$: Phonon engineering of metallic Ir and Rh. *Phys. Rev. B* **2021**, *104*, 054505. [CrossRef]
74. Horie, R.; Horigane, K.; Nishiyama, S.; Akimitsu, M.; Kobayashi, K.; Onari, S.; Kambe, T.; Kubozono, Y.; Akimitsu, J. Superconductivity in 5*d* transition metal Laves phase $SrIr_2$. *J. Phys. Condens. Matter* **2020**, *32*, 175703. [CrossRef]
75. Mao, Z.Q.; Rosario, M.M.; Nelson, K.D.; Wu, K.; Deac, I.G.; Schiffer, P.; Liu, Y.; He, T.; Regan, K.A.; Cava, R.J. Experimental determination of superconducting parameters for the intermetallic perovskite superconductor $MgCNi_3$. *Phys. Rev. B* **2003**, *67*, 094502. [CrossRef]
76. Ryżyńska, Z.; Chamorro, J.R.; McQueen, T.M.; Wiśniewski, P.; Kaczorowski, D.; Xie, W.; Cava, R.J.; Klimczuk, T.; Winiarski, M.J. $RuAl_6$—An endohedral aluminide superconductor. *Chem. Mater.* **2020**, *32*, 3805–3812. [CrossRef]
77. Langenberg, E.; Ferreiro-Vila, E.; Leborán, V.; Fumega, A.O.; Pardo, V.; Rivadulla, F. Analysis of the temperature dependence of the thermal conductivity of insulating single crystal oxides. *APL Mater.* **2016**, *4*, 104815. [CrossRef]
78. Adroja, D.; Bhattacharyya, A.; Biswas, P.K.; Smidman, M.; Hillier, A.D.; Mao, H.; Luo, H.; Cao, G.-H.; Wang, Z.; Wang, C. Multigap superconductivity in ThAsFeN investigated using μSR measurements. *Phys. Rev. B* **2017**, *96*, 144502. [CrossRef]
79. Albedah, M.A.; Nejadsattari, F.; Stadnik, Z.M.; Wang, Z.-C.; Wang, C.; Cao, G.H. Absence of the stripe antiferromagnetic order in the new 30 K superconductor ThFeAsN. *J. Alloys Compd.* **2017**, *695*, 1128–1136. [CrossRef]
80. Bhattacharyya, A.; Adroja, D.T.; Smidman, M.; Anand, V.K. A brief review on μSR studies of unconventional Fe- and Cr-based superconductors. *Sci. China Phys. Mech. Astron.* **2018**, *61*, 127402. [CrossRef]
81. Sonier, J.E.; Sabok-Sayr, S.A.; Callaghan, F.D.; Kaiser, C.V.; Pacradouni, V.; Brewer, J.H.; Stubbs, S.L.; Hardy, W.N.; Bonn, D.A.; Liang, R.; et al. Hole-doping dependence of the magnetic penetration depth and vortex core size in $YBa_2Cu_3O_y$: Evidence for stripe correlations near 1/8 hole doping. *Phys. Rev. B* **2007**, *76*, 134518. [CrossRef]
82. Kiefl, R.F.; Hossain, M.D.; Wojek, B.M.; Dunsiger, S.R.; Morris, G.D.; Prokscha, T.; Salman, Z.; Baglo, J.; Bonn, D.A.; Liang, R.; et al. Direct measurement of the London penetration depth in $YBa_2Cu_3O_{6.92}$ using low-energy μSR. *Phys. Rev. B* **2010**, *81*, 180502. [CrossRef]
83. Uemura, Y.J. Muon spin relaxation studies on high- T_c organic, heavy-fermion, and Chevrel phase superconductors. *Physical B* **1991**, *169*, 99–106. [CrossRef]
84. Talantsev, E.F.; Tallon, J.L. Universal self-field critical current for thin-film superconductors. *Nat. Commun.* **2015**, *6*, 7820. [CrossRef]
85. Talantsev, E.; Crump, W.P.; Tallon, J.L. Thermodynamic parameters of single- or multi-band superconductors derived from self-field critical currents. *Ann. Der Phys.* **2017**, *529*, 1700197. [CrossRef]
86. Wagner, P.; Hillmer, F.; Frey, U.; Adrian, H. Thermally activated flux movement and critical transport current density in epitaxial $Bi_2Sr_2CaCu_2O_{8+\delta}$ films. *Phys. Rev. B* **1994**, *49*, 13184. [CrossRef]
87. Holstein, W.L.; Wilker, C.; Laubacher, D.B.; Face, D.W.; Pang, P.; Warrington, M.S.; Carter, C.F.; Parisi, L.A. Critical current density and resistivity measurements for long patterned lines in $Tl_2Ba_2CaCu_2O_8$ thin films. *J. Appl. Phys.* **1993**, *74*, 1426–1430. [CrossRef]
88. Ledbetter, H. Dependence of on Debye temperature θ_D for various cuprates. *Phys. C* **1994**, *235–240*, 1325–1326. [CrossRef]
89. Krusin-Elbaum, L.; Tsuei, C.C.; Gupta, A. High current densities above 100 K in the high-temperature superconductor $HgBa_2CaCu_2O_{6+\delta}$. *Nature* **1995**, *373*, 679–681. [CrossRef]
90. Hänisch, J.; Attenberger, A.; Holzapfel, B.; Schultz, L. Electrical transport properties of $Bi_2Sr_2Ca_2Cu_3O_{10+\delta}$ thin film [001] tilt grain boundaries. *Phys. Rev. B* **2002**, *65*, 052507. [CrossRef]
91. Cava, R.J.; Batlogg, B.; Krajewski, J.J.; Farrow, R.; Rupp, L.W.; White, A.E.; Short, K.; Peck, W.F.; Kometani, T. Superconductivity near 30 K without copper: The $Ba_{0.6}K_{0.4}BiO_3$ perovskite. *Nature* **1988**, *332*, 814–816. [CrossRef]
92. Uemura, Y.J.; Luke, G.M.; Sternlieb, B.J.; Brewer, J.H.; Carolan, J.F.; Hardy, W.N.; Kadono, R.; Kempton, J.R.; Kiefl, R.F.; Kreitzman, S.R. Universal correlations between T_c and $\frac{n_S}{m^*}$ (carrier density over effective mass) in high-T_c cuprate. *Phys. Rev. Lett.* **1989**, *62*, 2317–2320. [CrossRef]
93. Szczesniak, D.; Kaczmarek, A.Z.; Drzazga-Szczesniak, E.A.; Szczesniak, R. Phonon-mediated superconductivity in bismuthates by nonadiabatic pairing. *Phys. Rev. B* **2021**, *104*, 094501. [CrossRef]
94. Hundley, M.F.; Thompson, J.D.; Kwei, G.H. Specific heat of the cubic high-T_c superconductor $Ba_{0.6}K_{0.4}BiO_3$. *Solid State Commun.* **1989**, *70*, 1155–1158. [CrossRef]
95. Cao, Y.; Fatemi, V.; Fang, S.; Watanabe, K.; Taniguchi, T.; Kaxiras, E.; Jarillo-Herrero, P. Unconventional superconductivity in magic-angle graphene superlattices. *Nature* **2018**, *556*, 43–50. [CrossRef]

96. Talantsev, E.F.; Mataira, R.C.; Crump, W.P. Classifying superconductivity in Moiré graphene superlattices. *Sci. Rep.* **2020**, *10*, 212. [CrossRef]
97. Cocemasov, A.I.; Nika, D.L.; Balandin, A.A. Engineering of the thermodynamic properties of bilayer graphene by atomic plane rotations: The role of the out-of-plane phonons. *Nanoscale* **2015**, *7*, 12851. [CrossRef]
98. Ludbrook, B.M.; Levy, G.; Nigge, P.; Zonno, M.; Schneider, M.; Dvorak, D.J.; Veenstra, C.N.; Zhdanovich, S.; Wong, D.; Dosanjh, P.; et al. Evidence for superconductivity in Li-decorated monolayer graphene. *Proc. Natl. Acad. Sci. USA* **2015**, *112*, 11795–11799. [CrossRef]
99. Szczesniak, D.; Szczesniak, R. Signatures of nonadiabatic superconductivity in lithium-decorated graphene. *Phys. Rev. B* **2019**, *99*, 224512. [CrossRef]
100. Park, S.; Kim, S.Y.; Kim, H.K.; Kim, M.J.; Kim, T.; Kim, H.; Choi, G.S.; Won, C.J.; Kim, S.; Kim, K.; et al. Superconductivity emerging from a stripe charge order in $IrTe_2$ nanoflakes. *Nat. Commun.* **2021**, *12*, 3157. [CrossRef]
101. Eremets, M.I.; Shimizu, K.; Kobayashi, T.C.; Amaya, K. Metallic CsI at pressures of up to 220 gigapascals. *Science* **1998**, *281*, 1333–1335. [CrossRef]
102. Talantsev, E.F. Fermi-liquid nonadiabatic highly compressed cesium iodide superconductor. *Condens. Matter* **2022**, *7*, 65. [CrossRef]
103. Talantsev, E.F. The dominance of non-electron–phonon charge carrier interaction in highly-compressed superhydrides. *Supercond. Sci. Technol.* **2021**, *34*, 115001. [CrossRef]
104. Talantsev, E.F. Universal Fermi velocity in highly compressed hydride superconductors. *Mater. Radiat. Extrem.* **2022**, *7*, 058403. [CrossRef]
105. Talantsev, E.F. Electron–phonon coupling constant and BCS ratios in LaH_{10-y} doped with magnetic rare-earth element. *Supercond. Sci. Technol.* **2022**, *35*, 095008. [CrossRef]
106. Shimizu, K.; Suhara, K.; Ikumo, M.; Eremets, M.I.; Amaya, K. Superconductivity in oxygen. *Nature* **1998**, *393*, 767–769. [CrossRef]
107. Talantsev, E.F. An approach to identifying unconventional superconductivity in highly compressed superconductors. *Supercond. Sci. Technol.* **2020**, *33*, 124001. [CrossRef]
108. Sebastian, S.E.; Harrison, N.; Lonzarich, G.G. Towards resolution of the Fermi surface in underdoped high-T_c superconductors. *Rep. Prog. Phys.* **2012**, *75*, 102501. [CrossRef]
109. Hsua, Y.-T.; Hartstein, M.; Davies, A.J.; Hickey, A.J.; Chan, M.K.; Porras, J.; Loew, T.; Taylor, S.V.; Liua, H.; Eaton, A.G.; et al. Unconventional quantum vortex matter state hosts quantum oscillations in the underdoped high-temperature cuprate superconductors. *Proc. Natl. Acad. Sci. USA* **2021**, *118*, e2021216118. [CrossRef]
110. Padilla, W.J.; Lee, Y.S.; Dumm, M.; Blumberg, G.; Ono, S.; Segawa, K.; Komiya, S.; Ando, Y.; Basov, D.N. Constant effective mass across the phase diagram of high-T_c cuprates. *Phys. Rev. B* **2005**, *72*, 060511. [CrossRef]
111. Talantsev, E.F.; Crump, W.P. Weak-links criterion for pnictide and cuprate superconductors. *Supercond. Sci. Technol.* **2018**, *31*, 124001. [CrossRef]
112. Paturi, P.; and Huhtinen, H. Roles of electron mean free path and flux pinning in optimizing the critical current in YBCO superconductors. *Supercond. Sci. Technol.* **2022**, *35*, 065007. [CrossRef]